Optomechanical Magnetometry with a Macroscopic Resonator

Changqiu Yu,[1,2] Jiri Janousek,[3] Eoin Sheridan,[2] David L. McAuslan,[2] Halina Rubinsztein-Dunlop,[2] Ping Koy Lam,[3] Yundong Zhang,[1] and Warwick P. Bowen[2,*]

[1]*National Key Laboratory of Tunable Laser Technology, Institute of Opto-Electronics, Harbin Institute of Technology, Harbin 150080, China*

[2]*Australian Centre for Engineered Quantum Systems, School of Mathematics and Physics, University of Queensland, Brisbane, Queensland 4072, Australia*

[3]*Centre for Quantum Computation and Communication Technology, Research School of Physics and Engineering, The Australian National University, Canberra, Australian Capital Territory 2601, Australia*

(Received 4 October 2015; revised manuscript received 9 January 2016; published 15 April 2016)

We demonstrate a centimeter-scale optomechanical magnetometer based on a crystalline whispering-gallery-mode resonator. The large size of the resonator, with a magnetic-field integration volume of 0.45 cm^3, allows high magnetic-field sensitivity to be achieved in the hertz-to-kilohertz frequency range. A peak sensitivity of 131 pT $Hz^{-1/2}$ is reported, in a magnetically unshielded noncryogenic environment using optical power levels beneath 100 μW. Femtotesla-range sensitivity may be possible in future devices with the further optimization of laser noise and the physical structure of the resonator, allowing applications in high-performance magnetometry.

DOI: 10.1103/PhysRevApplied.5.044007

I. INTRODUCTION

Whispering-gallery-mode (WGM) resonators play an important role in modern optics, with applications as laser cavities [1], resonant filters [2], optical switches [3], and precision sensors [4–7] among other areas. They have been recently used for magnetometry [8,9] based on the ideas of cavity optomechanics [10]. WGM-resonator-based optomechanical magnetometry combines the ultrahigh optical-transduction sensitivity of WGM resonators with the giant magnetostriction of materials such as Terfenol-D, achieving high sensitivity while allowing room-temperature operation, low optical power levels, and simple all-optical readout. Theoretical modeling indicates that future fully optimized devices that attain the fundamental thermomechanical noise floor may achieve sensitivity in the low, or even sub-, femtotesla range [11]. These advantages provide a pathway towards potential future applications in areas such as geophysical surveying [12], tests of fundamental physics [13,14], medical imaging [15,16], and space exploration [17,18].

Optomechanical magnetometers based on microscale on-chip WGM resonators achieve 200 pT $Hz^{-1/2}$ magnetic-field sensitivity at megahertz frequencies [8,9]. However, due to a combination of noise sources at low frequency and a poor low-frequency mechanical response, magnetic-field sensing in the hertz-to-kilohertz frequency range was possible only by using inherent mechanical nonlinearities within the magnetostrictive material [9]. This indirect approach causes a sacrifice in sensitivity to 110 nT $Hz^{-1/2}$. The hertz-to-kilohertz frequency range is crucial to many applications including, for instance, magnetic-anomaly detection [19], geological surveying [20], and magnetoencephalography [16]. To enable highly sensitive magnetic-field sensing in this regime, we develop a centimeter-scale crystalline WGM-resonator-based magnetometer, which features reduced thermomechanical noise, lower-frequency mechanical resonances, and a higher optical-quality factor than previously demonstrated optomechanical magnetometers. By embedding the magnetostrictive material (Terfenol-D) within the WGM resonator, sub-10-nT $Hz^{-1/2}$ sensitivity is achieved over most of the frequency band from 127 Hz to 600 kHz, with a peak sensitivity of 131 pT $Hz^{-1/2}$ at 127 kHz.

II. RESONATOR FABRICATION AND CHARACTERIZATION

The WGM resonator is fabricated by using the Ultra-precision Machining Facility at the Australian National University, housing a Moore Nanotech 250 UPL diamond turning lathe. WGM resonators are particularly well suited for fabrication by diamond turning due to their cylindrical symmetry. We fabricate the resonator from CaF_2 due, primarily, to the previously demonstrated capability to achieve exceptionally high optical-quality factors by using this material [21]. We expect that similar results to those reported here could alternatively be achieved by using other materials such as quartz [22], lithium niobate [23], or magnesium fluoride [24]. The fabrication process of the magnetometer is shown in Fig. 1(a). A bulk of CaF_2 crystal, which is attached to a ceramic pedestal by using a vacuum-compatible epoxy glue (EPO-TEX 353ND), is first rough cut to form a WGM resonator with a diameter of 16 mm. Lathing is also used to bore a void in the top of the crystal

*w.bowen@uq.edu.au

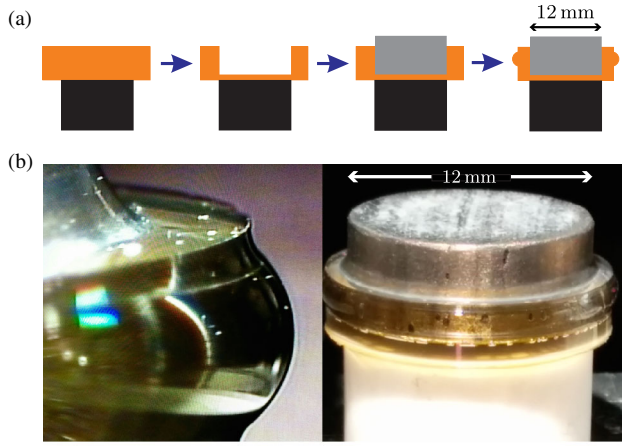

FIG. 1. (a) The fabrication process. Black area, ceramic; yellow area, CaF_2; gray area, Terfenol-D (Etrema products, Inc.). (b) Optical microscope images of the resonator.

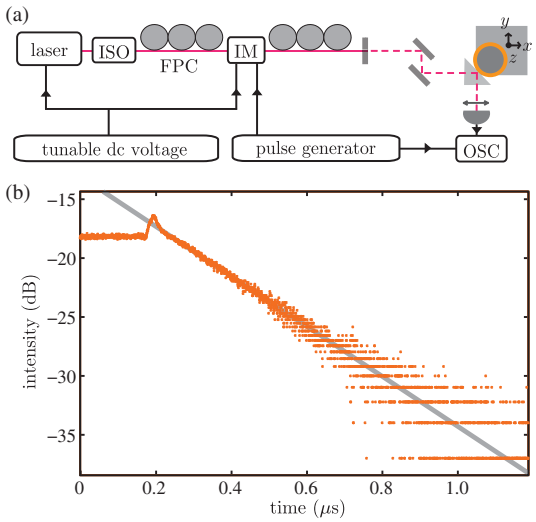

FIG. 2. Ringdown measurements. (a) Schematic of the apparatus used to perform the ringdown measurement of the optical-quality factor. FPC, fiber polarization controller; IM, intensity modulator (OC-192 Modulator JDS Uniphase); OSC, oscilloscope (Tektronix TDS 2024B), pulse generator (Stanford DG535), nanomax stage (Thorlabs MDT693A), prism (uncoated N-BK7 right-angle prism), and detector (New Focus Model-1811). (b) Plot of the relative detected optical intensity, with the electro-optic modulator (EOM) used to shutter the optical field at approximately 175 ns. The solid gray curve is an exponential fit to the data over the range 221–454 ns.

WGM structure. The void is machined to a diameter 30 μm larger than the actual size of the disk of Terfenol-D (of diameter and thickness approximately 12 and 4 mm, respectively, resulting in a magnetic-field integration volume of 0.45 cm^3). The 15-μm gap is the minimum that allows the epoxy glue, due to its viscosity, to uniformly fill the interface of the two materials. Next, we machine the final WGM structure with a radius of curvature of the resonator's rim of 1.616 mm [25].

The final step is to polish the resonator to achieve an extremely smooth surface, i.e., a high intrinsic optical-quality factor. By using the lathe to rotate the WGM resonator and ensure that the resonator is precisely centered on the rotational axis, polishing is accomplished with a polishing pad and diamond slurry. Starting with a 0.5-μm particle size, large chips on the surface of the resonator left after cutting are removed, and, by using progressively smaller particle sizes down to 0.05 μm, the final polishing is achieved. The physical structure of the resonator is shown in Fig. 1(b).

The optical-quality factor of the WGM resonator is characterized via a cavity-ringdown measurement [26], using the setup shown in Fig. 2(a). Alternatively, the quality factor could be determined by sweeping the laser frequency over the optical resonance and determining the linewidth of the resonance. Cavity ringdown is chosen here to avoid inaccuracies introduced both by thermo-optic effects, where optical heating of the resonator shifts its resonance frequencies and thereby modifies the observed line shapes [27], and by possible laser-frequency calibration errors. A fiber laser of wavelength $\lambda = 1550$ nm is critically coupled into the resonator by using a prism mounted on a three-axis nanopositioning stage. Critical coupling is achieved by locating the prism at a distance from the resonator which minimizes the power totally internally reflected from the prism surface and therefore maximizes the intraresonator power. An optical intensity modulator with a 35-ps rise or fall time and a 20-dB extinction ratio is used to rapidly switch off the laser intensity. The exponential decay of light out of the resonator is then detected by using a fast photodiode. The resulting cavity-ringdown measurement is shown in Fig. 2(b). The cavity lifetime τ_e is determined to be 233 ns from an exponential fit to the data [gray line in Fig. 2(b)], which corresponds to an intrinsic optical-quality factor of $Q \equiv \Omega\tau_e = 2\pi c\tau_e/\lambda = 2.8 \times 10^8$, where Ω is the angular frequency of the laser and c is the speed of light in a vacuum [28]. We note that this quality factor is significantly lower than the best reported quality factors for polished crystalline CaF_2 resonators [21]. Substantially higher-quality factors are observed on the initial alignment of the system, with degradation occurring due to surface imperfections introduced from repeated contact of the prism to the resonator surface. As discussed later, the quality factor is sufficiently high that our current experiments are limited by laser phase noise and mechanical characteristics rather than cavity quality.

III. EXPERIMENT

Figure 3 shows a schematic of the measurement setup. Light from the fiber laser is passed through an isolator and an EOM and then evanescently coupled to the resonator in the same manner as described in the previous section. The

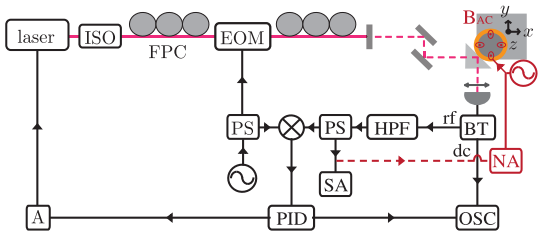

FIG. 3. A schematic of the experimental setup used to perform magnetic-field sensing. Laser (Koheras Adjustik C15); ISO, isolator (Thorlabs-OFR); EOM, electro-optic modulator (Covega phase modulator); NA, network analyzer (Agilent E5061B); SA, spectrum analyzer (Agilent N9010A); PID, proportional integral derivative controller (New Focus LB1005); BT, bias tee (mini circuits 0.1–4200 MHz); HPF, high-pass filter (mini circuits 0.07–1000 MHz); LPF, low-pass filter (mini circuits dc-1.9 MHz); PS, power splitter (mini circuits 1–650 MHz); and A, amplifier (ZFL-500).

EOM is used to phase modulate the light at 13.6 MHz, well outside the resonator's linewidth ($\kappa/2\pi = \tau_e^{-1}/2\pi <$ 1 MHz). The output field from the resonator is detected on an InGaAs photoreceiver. Electronic mixing of this output with a 13.6-MHz local oscillator generates a Pound-Drever-Hall (PDH) error signal [29]. This error signal provides a measure of the deviation of the laser frequency from the cavity-resonance frequency. In a similar approach to Ref. [30], this signal is used both to lock the laser to the cavity resonance and to detect the effect of applied magnetic fields on the length of the cavity—i.e., it provides the magnetic-field signal. To maximize the signal-to-noise ratio (SNR) of the sensor, a large modulation is applied to the EOM, transferring approximately half of the optical power into 13.6-MHz sidebands. It is found that only 40 μW of off-resonant light is required at the photoreceiver to resolve the noise of the optical field over the photoreceiver electronic noise floor. A coil with a diameter of 6.5 cm and a total of 60 turns is positioned above the resonator and used to generate the signal magnetic field to be detected. The strength of this field is calibrated by using a commercial Hall probe (Hirst GM04). A neodymium magnet is placed in close proximity to the resonator to prepolarize the Terfenol-D, thereby enhancing its linear response to applied magnetic fields [9,31].

IV. RESULTS AND DISCUSSION

The response of the magnetometer to applied signal fields is characterized via spectral and network analysis of the PDH error signal. Figure 4(a) shows the power spectral density $S(\omega)$ of the error signal at frequencies above the 13.6-MHz optical sideband frequency, measured by using a spectrum analyzer. This power spectral density constitutes the noise floor of our measurements. It is found to be relatively insensitive to the prism-resonator coupling rate via observations over a range of prism coupler positions

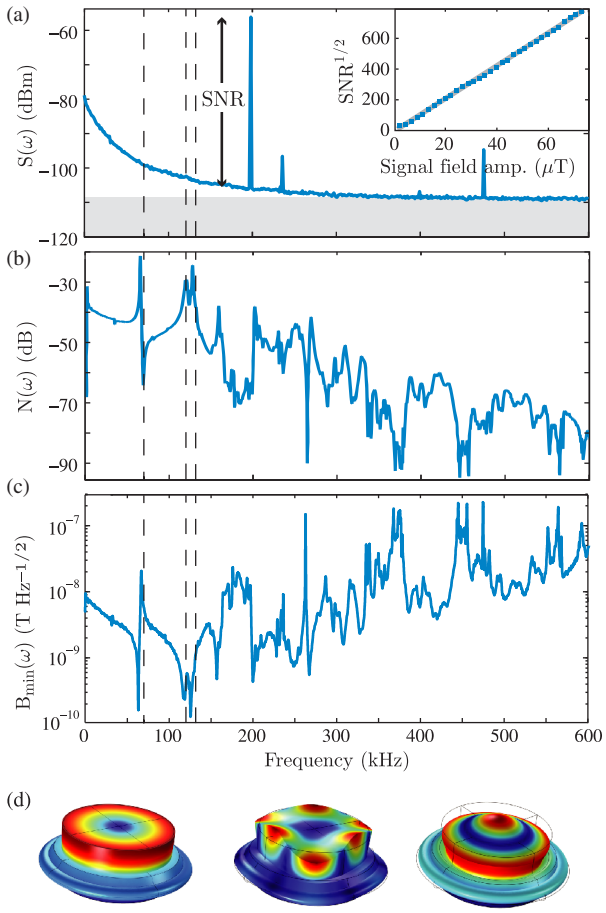

FIG. 4. Experimental results. (a) Power spectral density $S(\omega)$ of the error signal at offset frequencies above the 13.6-MHz optical sideband frequency, showing the response an applied magnetic field at 200 kHz. The gray-shaded region indicates the shot noise floor. Inset: Response to the magnetic field as a function of the signal-field strength, with a 330-Hz spectrum analyzer resolution bandwidth. (b) System response $N(\omega)$ measured via network analysis as a function of the applied magnetic-field frequency. (c) Magnetic-field sensitivity $B_{\min}(\omega)$ as a function of frequency. (d) Finite element modeling of mechanical eigenmodes of the device. From left to right, the modes are the fundamental radial breathing mode at 69.8 kHz, a crown mode at 120.4 kHz, and the second-order radial breathing mode at 131.9 kHz. The vertical dashed lines in (a)–(c) show the frequencies of these three modes.

away from critical coupling. Similarly, magnetic-field noise due to Barkhausen fluctuations within the neodymium magnet [32] is found to have no observable effect on the measurement noise floor via observations of the power spectral density as the magnet is displaced vertically.

It is verified that the resonator is capable of detecting magnetic fields by applying a reference magnetic field with root-mean-square (rms) amplitude $B_{\rm ref} = 7.8$ μT and frequency $\omega_{\rm ref} = 200$ kHz. This causes a corresponding tone at 200 kHz in the power spectral density of the error signal [see Fig. 4(a)]. The magnetic-field sensitivity at 200 kHz is then determined by following Ref. [8] as

$$B_{\min}(\omega_{\mathrm{ref}}) = \frac{B_{\mathrm{ref}}}{\sqrt{\mathrm{SNR} \times \mathrm{BW}}} = 1.4\ \mathrm{nT\,Hz^{-1/2}}, \quad (1)$$

where SNR = 49.7 dB is the ratio of the signal height at ω_{ref} to the corresponding noise floor [see Fig. 4(a)] and BW = 330 Hz is the spectrum analyzer resolution bandwidth. The dynamic range of the magnetometer is tested by measuring the response as a function of the signal-field amplitude. A linear response is observed over the full accessible range of signal-field strengths, up to field strengths as large as 72 μT, which exceeds Earth's field [see the inset in Fig. 4(a)].

The spectrum analyzer noise floor in Fig. 4(a) combined with the system response, as quantified by network analysis, allows the magnetic-field sensitivity to be determined over the full hertz-to-kilohertz frequency range. Specifically, the magnetic-field sensitivity is given by [8]

$$B_{\min}(\omega) = \sqrt{\frac{S(\omega)N(\omega_{\mathrm{ref}})}{S(\omega_{\mathrm{ref}})N(\omega)}} B_{\min}(\omega_{\mathrm{ref}}), \quad (2)$$

where $S(\omega)$ is the noise power spectrum observed without any applied magnetic field and $N(\omega)$ is the system response obtained by sweeping the frequency of the magnetic field and recording the power contained within the spectral peak using a network analyzer, shown in Fig. 4(b). Below 140 kHz, the structure in the system response is dominated by three mechanical eigenmodes of the device. Finite-element simulations of these modes are shown in Fig. 4(d), with the simulated frequencies matching closely to the observed frequencies evident in Fig. 4(b). Note that the dispersive feature at the fundamental radial breathing-mode-resonance frequency (69.8 kHz) results from interference of the response of that mode and the background response of the device. An inspection of the measured error signal power spectrum [Fig. 4(a)] shows that the thermomechanical noise of all of these three mechanical eigenmodes is beneath the laser phase noise floor, indicating that the precision of magnetic-field measurement with this device will be limited by laser noise rather than thermomechanical noise. Above 140 kHz, the system response is suppressed with increasing frequency, with a complex structure existing due to the presence of multifold higher-frequency mechanical resonances.

Figure 4(c) shows the sensitivity measured over the frequency range from 127 Hz to 600 kHz. A peak sensitivity of 131 $\mathrm{pT\,Hz^{-1/2}}$ is achieved at 126.75 kHz, close to the eigenfrequencies of the mechanical crown and second-order radial breathing modes, while similar sensitivity is also achievable at frequencies close to the fundamental radial breathing mode. Evidently, the sensitivity is enhanced by these mechanical resonances and outperforms previous cavity optomechanical magnetometers in the same frequency range by around 3 orders of magnitude. The best previously reported result has a sensitivity above 130 $\mathrm{nT\,Hz^{-1/2}}$ over the full range of the measurements we report here [9]. The sensitivity is within a factor of 2 of the peak sensitivity over a 5-kHz frequency band, defining the overall band width of the magnetometer.

The sensitivity of our current devices is constrained, predominantly, by the following two effects. First, the overlap between the magnetostrictive expansion caused by the magnetic field and the dominant mechanical eigenmodes of the physical structure [those shown in Fig. 4(d)] is not optimized; second, the optomechanical coupling between each of these eigenmodes and the phase of the intraresonator optical field is not ideal—this is evident in the small mechanical displacement in the circumference of the device relative to the maximum displacement in the finite element simulations of Fig. 4(d). Each of these effects could be greatly mitigated by engineering the physical structure of the device to optimize the shape of the mechanical eigenmodes. Optimization of this kind has already been shown to allow substantially improved performance in many other cavity optomechanical systems (see, for example, Refs. [33–35]). Optical noise also constrains the sensitivity. Below 200 kHz, laser phase noise is the dominant source of optical noise, while shot noise dominates above that frequency [see Fig. 4(a)]. Consequently, improved sensitivity could be achieved by using phase stabilization [36] and increased optical power, until eventually the thermomechanical noise of the mechanical eigenmodes dominates the optical noise and the thermomechanical noise floor is reached [8,9]. At frequencies where the sensitivity is limited by shot noise rather than laser phase noise, the sensitivity could be further enhanced by using a higher-Q resonator. Quality factors as high as $Q = 3 \times 10^{11}$ have been realized for a millimeter-scale CaF_2 WGM resonator at 1550 nm [21].

While the results presented here extend the capabilities of cavity optomechanical magnetometers considerably, it is still possible to achieve superior sensitivity with other approaches. For instance, 1-cm-diameter cryogenic superconducting interference (SQUID) magnetometers have been demonstrated with a sensitivity of 1.5 $\mathrm{fT\,Hz^{1/2}}$ [37]. Alternatively, atomic-ensemble-based spin-exchange relaxation-free (SERF) magnetometers allow all-optical precision magnetometry at room temperature, with subfemtotesla sensitivity demonstrated by using a 2.4-cm device [38]. This impressive performance comes with the associated complexity of laser pumping as well as a dynamic range limited well beneath Earth's field [39]. Commercial room-temperature electrical magnetometers reduce sensitivity compared to these high-performance counterparts but offer the advantages of being robust, inexpensive, and easily integrated with other electrical systems. Sensitivities as high as 100 $\mathrm{fT\,Hz^{-1/2}}$ (Phoenix Geophysics, MTC-50) and 6 $\mathrm{pT\,Hz^{-1/2}}$ (Bartington, MAG-03) are available using induction coil and flux gate magnetometers, respectively, with size scales of a few centimeters.

From the discussion in the preceding paragraph, it should be clear that substantial further improvements are required

for cavity optomechanical magnetometers to compete in terms of absolute precision with existing magnetometers, both high performance and commercial. Above and beyond the progress reported here, a 3-orders-of-magnitude improvement in peak sensitivity is necessary to achieve a comparable performance to the best commercial induction coil magnetometers, putting aside the technical advantages of electrical readout. A further 2 orders of magnitude are required to compete—on precision—with SQUID and SERF magnetometers. At frequencies away from the mechanical resonances, more substantial improvements are required. For instance, more than an order-of-magnitude reduction in sensitivity is observed at frequencies below a kilohertz, a frequency band relevant to many applications. This highlights a second limitation of our magnetometer, that, due to the reliance on relatively high-quality mechanical resonances, the response of the sensor is not flat with the sensitivity varying by several orders of magnitude across the measured frequency range. We note, however, that this sensitivity variation is not fundamental to our magnetometer design. It arises when optical noise is the primary factor limiting the sensitivity. Future devices that achieve thermal-noise-limited performance at frequencies beneath the mechanical resonance frequency and have a single dominant mechanical mode would allow uniform sensitivity to be achieved at all frequencies up to the mechanical resonance [11]. This would allow bandwidths in the range of hundreds of kilohertz, competitive with commercial magnetometers and substantially larger than the kilohertz bandwidth typical of SERF magnetometers [38].

The substantial improvements in precision required to compete with commercial and state-of-the-art magnetometers are predicted to be achievable with the approach to magnetometry demonstrated here [11]. Optimized devices of a similar design to those reported here, operating at the thermomechanical noise limit, could in principle achieve a sensitivity at the level of 10 $\mathrm{fT\,Hz^{-1/2}}$, while subfemtotesla precision is predicted to be possible for alternative designs based on the measurement of a vertical, rather than radial, magnetostrictive expansion. In the latter case, the vertical material expansion could be measured, for instance, by using a macroscale double-disk whispering-gallery-mode resonator similar to that in Ref. [40], which provides the additional benefit of considerably larger optomechanical coupling compared to a single whispering-gallery-mode resonator. We further emphasize that cavity optomechanical devices have the technical advantages of operating in both Earth-field and room-temperature environments, combined with microwatt optical power requirements and intrinsically low electromagnetic interference due to their all-optical design.

ACKNOWLEDGMENTS

The authors acknowledge valuable advice from Beibei Li, Glen Harris, George Brawley, and Michael Taylor. This research is funded by the Australian Research Council Centre of Excellences CE110001013 and CE110001027, the Discovery Project DP140100734, and DARPA via a grant through the ARO. Device fabrication was performed at the Australian National University. C. Y. acknowledges support by the China Scholarship Council (File No. LJF [2013]3009). W. P. B. and P. K. L. are supported by the ARC Future and Laureate Fellowship FT140100650 and FL150100019, respectively.

[1] V. Sandoghdar, F. Treussart, J. Hare, V. Lefevre-Seguin, J. M. Raimond, and S. Haroche, Very low threshold whispering-gallery-mode microsphere laser, Phys. Rev. A **54**, R1777 (1996).

[2] F. Monifi, S. K. Ozdemir, and L. Yang, Tunable add-drop filter using an active whispering gallery mode microcavity, Appl. Phys. Lett. **103**, 181103 (2013).

[3] A. Eschmann and C. W. Gardiner, Stability and switching in whispering-gallery-mode microdisk lasers, Phys. Rev. A **49**, 2907 (1994).

[4] M. Noto, M. Khoshsima, D. Keng, I. Teraoka, V. Kolchenko, and S. Arnold, Molecular weight dependence of a whispering gallery mode biosensor, Appl. Phys. Lett. **87**, 223901 (2005).

[5] B.-B. Li, W. R. Clements, X. C. Yu, K. Shi, Q. Gong, and Y.-F. Xiao, Single nanoparticle detection using split-mode microcavity Raman lasers, Proc. Natl. Acad. Sci. U.S.A. **111**, 14657 (2014).

[6] F. Sedlmeir, R. Zeltner, G. Leuchs, and H. G. Schwefel, High-Q MgF_2 whispering gallery mode resonators for refractometric sensing in aqueous environment, Opt. Express **22**, 30934 (2014).

[7] W. Weng, J. D. Anstie, T. M. Stace, G. Campbell, F. N. Baynes, and A. N. Luiten, Nano-Kelvin Thermometry and Temperature Control: Beyond the Thermal Noise Limit, Phys. Rev. Lett. **112**, 160801 (2014).

[8] S. Forstner, S. Prams, J. Knittel, E. D. van Ooijen, J. D. Swaim, G. I. Harris, A. Szorkovszky, W. P. Bowen, and H. Rubinsztein-Dunlop, Cavity Optomechanical Magnetometer, Phys. Rev. Lett. **108**, 120801 (2012).

[9] S. Forstner, E. Sheridan, J. Knittel, C. L. Humphreys, G. A. Brawley, H. Rubinsztein-Dunlop, and W. P. Bowen, Ultrasensitive optomechanical magnetometry, Adv. Mater. **26**, 6348 (2014).

[10] M. Aspelmeyer, T. J. Kippenberg, and F. Marquardt, Rev. Mod. Phys. **86**, 1391 (2014).

[11] *High Sensitivity Magnetometers*, Springer Series on Smart Sensors, Measurement and Instrumentation, edited by A. Grosz, M. J. Haji-Sheikh, and S. C. Mukhopadhyay (Springer, New York, 2016).

[12] M. N. Nabighian, V. J. S. Grauch, R. O. Hansen, T. R. LaFehr, Y. Li, W. C. Pearson, J. W. Peirce, J. D. Phillips, and M. E. Ruder, 75th Anniversary: The historical development of the magnetic method in exploration, Geophysics **70**, 33ND (2005).

[13] B. Plaster, Search for the neutron electric dipole moment, AIP Conf. Proc. **1265**, 300 (2010).

[14] C. A. Baker *et al.*, CryoEDM: A cryogenic experiment to measure the neutron electric dipole moment, J. Phys. Conf. Ser. **251**, 012055 (2010).

[15] I. Savukov and T. Karaulanov, Magnetic-resonance imaging of the human brain with an atomic magnetometer, Appl. Phys. Lett. **103**, 043703 (2013).
[16] H. Xia, A. Ben-Amar Baranga, D. Hoffman, and M. V. Romalis, Magnetoencephalography with an atomic magnetometer, Appl. Phys. Lett. **89**, 211104 (2006).
[17] H. Zhao, G. W. Zhu, P. Yu, J. D. Wang, M. F. Yu, L. Li, Y. Q. Sun, S. W. Chen, H. Z. Liao, B. Zhou, and Y. Y. Feng, Fluxgate magnetometer for Mars exploration, Proc. SPIE Int. Soc. Opt. Eng. **7129**, 71292N (2008).
[18] W. Magnes, D. Pierce, A. Valavanoglou, J. Means, W. Baumjohann, C. T. Russell, K. Schwingenschuh, and G. Graber, A sigma-delta fluxgate magnetometer for space applications, Meas. Sci. Technol. **14**, 1003 (2003).
[19] J. Zhai, Z. Xing, S. Dong, J. Li, and D. Viehland, Detection of pico-Tesla magnetic fields using magneto-electric sensors at room temperature, Appl. Phys. Lett. **88**, 062510 (2006).
[20] H. G. Meyer, R. Stolz, A. Chwala, and M. Schulz, SQUID technology for geophysical exploration, Phys. Status Solidi (a) **2**, 1504 (2005).
[21] A. A. Savchenkov, A. B. Matsko, V. S. Ilchenko, and L. Maleki, Optical resonators with ten million finesse, Opt. Express **15**, 6768 (2007).
[22] V. S. Ilchenko, A. A. Savchenkov, J. Byrd, I. Solomatine, A. B. Matsko, D. Seidel, and L. Maleki, Crystal quartz optical whispering-gallery resonators, Opt. Lett. **33**, 1569 (2008).
[23] A. B. Matsko, A. A. Savchenkov, D. Strekalov, V. S. Ilchenko, and L. Maleki, Review of applications of whispering-gallery mode resonators in photonics and nonlinear optics, IPN Prog. Rep. **42**, 162 (2005).
[24] H. Tavernier, P. Salzenstein, K. Volyanskiy, Y. K. Chembo, and L. Larger, Magnesium fluoride whispering gallery mode disk-resonators for microwave photonics applications, IEEE Photonics Technol. Lett. **22**, 1629 (2010).
[25] D. V. Strekalov, A. A. Savchenkov, A. B. Matsko, and N. Yu, Efficient upconversion of subterahertz radiation in a high-Q whispering gallery resonator, Opt. Lett. **34**, 713 (2009).
[26] D. K. Armani, T. J. Kippenberg, S. M. Spillane, and K. J. Vahala, Ultrahigh-Q toroid microcavity on a chip, Nature (London) **421**, 925 (2003).
[27] H. Rokhsari, S. M. Spillane, and K. J. Vahala, Loss characterization in microcavities using the thermal bistability effect, Appl. Phys. Lett. **85**, 3029 (2004).
[28] A. A. Savchenkov, A. B. Matsko, M. Mohageg, and L. Maleki, Ringdown spectroscopy of stimulated Raman scattering in a whispering gallery mode resonator, Opt. Lett. **32**, 497 (2007).
[29] E. D. Black, An introduction to Pound-Drever-Hall laser frequency stabilization, Am. J. Phys. **69**, 79 (2001).
[30] J. D. Swaim, J. Knittel, and W. P. Bowen, Detection of nanoparticles with a frequency locked whispering gallery mode microresonator, Appl. Phys. Lett. **102**, 183106 (2013).
[31] G. Engdahl, *Handbook of Giant Magnetostrictive Materials* (Academic, New York, 2000).
[32] C. G. Stefanita, *From Bulk to Nano: The Many Sides of Magnetism* (Springer, New York, 2008), pp. 19–40.
[33] G. Anetsberger, R. Rivière, A. Schliesser, O. Arcizet, and T. J. Kippenberg, Ultralow-dissipation optomechanical resonators on a chip, Nat. Photonics **2**, 627 (2008).
[34] M. Eichenfield, J. Chan, R. M. Camacho, K. J. Vahala, and O. Painter, Optomechanical crystals, Nature (London) **462**, 78 (2009).
[35] G. D. Cole, I. Wilson-Rae, K. Werbach, M. R. Vanner, and M. Aspelmeyer, Phonon-tunnelling dissipation in mechanical resonators, Nat. Commun. **2**, 231 (2011).
[36] T. Lu, H. Lee, T. Chen, S. Herchak, J. H. Kim, S. E. Fraser, R. C. Flagan, and K. Vahala, High sensitivity nanoparticle detection using optical microcavities, Proc. Natl. Acad. Sci. U.S.A. **108**, 5976 (2011).
[37] R. L. Fagaly, Superconducting quantum interference device instruments and applications, Rev. Sci. Instrum. **77**, 101101 (2006).
[38] H. B. Dang, A. C. Maloof, and M. V. Romalis, Ultrahigh sensitivity magnetic field and magnetization measurements with an atomic magnetometer, Appl. Phys. Lett. **97**, 151110 (2010).
[39] D. Budker and D. F. Kimball, *Optical Magnetometry* (Cambridge University Press, Cambridge, England, 2013).
[40] Q. Lin, J. Rosenberg, X. Jiang, K. J. Vahala, and O. Painter, Mechanical Oscillation and Cooling Actuated by the Optical Gradient Force, Phys. Rev. Lett. **103**, 103601 (2009).